Nanoporous Submicron Gold Particles Enable Nanoparticle-Based Localization Optoacoustic Tomography (nanoLOT)

Daniil Nozdriukhin, Marco Cattaneo, Norman Klingler, Shuxin Lyu, Weiye Li, Francisco Montero de Espinosa, Jerome Bonvin, Outi Supponen, Daniel Razansky, and Xosé Luís Deán-Ben*

Localization optoacoustic tomography (LOT) has recently emerged as a transformative super-resolution technique breaking through the acoustic diffraction limit in deep-tissue optoacoustic (OA) imaging via individual localization and tracking of particles in the bloodstream. However, strong light absorption in red blood cells has previously restricted per-particle OA detection to relatively large microparticles, ≈5 μm in diameter. Herein, it is demonstrated that submicron-sized porous gold nanoparticles, ≈600 nm in diameter, can be individually detected for noninvasive super-resolution imaging with LOT. Ultra-high-speed bright-field microscopy revealed that these nanoparticles generate microscopic plasmonic vapor bubbles, significantly enhancing opto-acoustic energy conversion through a nano-to-micro size transformation. Comprehensive in vitro and in vivo tests further demonstrated the biocompatibility and biosafety of the particles. By reducing the detectable particle size by an order of magnitude, nanoLOT enables microangiographic imaging with a significantly reduced risk of embolisms from particle aggregation and opens new avenues to visualize how nanoparticles reach vascular and potentially extravascular targets. The performance of nanoLOT for non-invasive imaging of microvascular networks in the murine brain anticipates new insights into neurovascular coupling mechanisms and longitudinal microcirculatory changes associated with neurodegenerative diseases.

1. Introduction

Super-resolution approaches have been implemented in optical microscopy and other imaging modalities to visualize microscopic structures with unprecedented detail.[1–6] Expanding the scope of distinguishable features in biomedical images can improve clinical diagnostic capacities and deepen our understanding of biological function.[7] Localization-based super-resolution imaging, which relies on precise determination of the positions of individual sources, is a powerful approach to overcome the longstanding diffraction limits on spatial resolution. Optical microscopy first capitalized on this principle to visualize subcellular processes at the nanoscale from localized temporally-separated activated fluorescent molecules.[8,9] Ultrasound (US) was subsequently developed as a super-resolution angiographic imaging method based on localization and tracking of individual microbubbles in the bloodstream.[10–12]

D. Nozdriukhin, S. Lyu, W. Li, J. Bonvin, D. Razansky, X. L. Deán-Ben
Institute for Biomedical Engineering and Institute of Pharmacology and Toxicology, Faculty of Medicine
University of Zürich
Winterthurerstrasse 190, Zurich 8057, Switzerland
E-mail: xl.deanben@pharma.uzh.ch

D. Nozdriukhin, S. Lyu, W. Li, J. Bonvin, D. Razansky, X. L. Deán-Ben
Institute for Biomedical Engineering, Department of Information Technology and Electrical Engineering
ETH Zürich
Rämistrasse 101, Zurich 8093, Switzerland

M. Cattaneo, N. Klingler, O. Supponen
Institute of Fluid Dynamics, Department of Mechanical and Process Engineering
ETH Zürich
Sonneggstrasse 3, Zurich 8092, Switzerland

S. Lyu
Department of Medical Imaging
Shanxi Medical University
Xinjiannan Road 56, Shanxi 030001, China

F. M. de Espinosa
Institute of Physics and Communication Technologies
CSIC
Serrano 144, Madrid 28006, Spain

**ADVANCED
SCIENCE NEWS**

www.advancedsciencenews.com

NANO · MICRO

small

www.small-journal.com

Biomedical optoacoustic (OA, photoacoustic) imaging was first demonstrated around two decades ago and has remarkably evolved to become a powerful tool in biology and medicine.[13] Recently, localization optoacoustic tomography (LOT) has been proposed to break through the acoustic diffraction barrier while further capitalizing on the unique OA advantages stemming from the synergistic combination between light and sound.[14–17] Indeed, OA enables attaining high-resolution functional and molecular contrast unaffected by optical diffusion in deep tissues. LOT further expands the resolution-depth range via angiographic and blood velocity mapping in a similar fashion as super-resolution US imaging while additionally providing label-free oxygen saturation readings.[18] This unique multi-parametric imaging performance combined with the powerful capacity of OA to visualize a myriad of optical contrast agents has significant potential to advance studies in oncology, neuroscience, metabolism, and other fields.[19–21]

The successful implementation of LOT has been challenged by the lack of intravenously injectable contrast agents providing sufficient signal on a per-particle basis to be individually detected in vivo amid strongly absorbing blood background.[22] Indeed, red blood cells (RBCs) occupy ≈50% of blood volume and feature higher per-unit light absorption compared to dye molecules or nanoparticles commonly used as OA contrast agents. LOT has previously been achieved with dichloromethane droplets with diameters of ≈5 μm encapsulating a highly concentrated near-infrared dye. This enabled achieving total optical absorption exceeding that of RBCs by several orders of magnitude.[18] Layer-by-layer coated silica particles with similar sizes could also be individually detected in vivo,[23,24] while larger particles were shown to result in capillary arrest.[25] Indeed, potential aggregation of particles may cause embolisms restricting blood flow to tissues or organs potentially causing damage or dysfunction. Relatively large particles are also known to be easily recognizable by phagocytic cells of the reticuloendothelial system,[26,27] while they also remain in the blood circulation without reaching extravascular targets.[28]

Gold-based nanoparticles are known to provide extraordinary light absorption properties and have demonstrated excellent performance as OA contrast agents.[29–31] Their absorption spectrum and absorption peak can be tuned by altering the size, shape, and structural complexity, which can be achieved by varying synthesis parameters.[32–34] For example, sharp edges or nanogaps within and between the particles or particle clusters tend to concentrate the electromagnetic field to effectively increase plasmonic light absorption.[35,36] On the other hand, a structured surface can act as a substrate for plasmonic coupling resulting in red-shifted absorption.[37,38] These effects were exploited for synthesizing porous gold nanoparticles of submicron size to boost the detected signals in surface-enhanced Raman scattering.[39] These particles are mainly produced on templates of organic beads or silver cubes,[40,41] with one-pot synthesis methods also suggested.[37,42]

In this study, we demonstrate the potential of using submicron porous gold nanoparticles for angiographic imaging with motion contrast optoacoustic (MC-OA) imaging and super-resolution localization optoacoustic tomography (LOT). We thoroughly characterized the synthesized nanoparticles using a variety of optical and OA techniques, including OA microscopy, OA tomography, and ultra-high-speed bright-field microscopy. Ultra-high-speed imaging revealed that bubble formation resulting from plasmonic cavitation induced with a short-pulsed laser serves as a fundamental mechanism for efficient ultrasound generation. Additionally, in vitro and in vivo toxicity assays indicate that these nanoparticles do not cause observable toxic effects and can be safely administered to mice. Particle-induced fluctuations in the OA images of the murine brain vasculature facilitated reconstruction of cerebral vessel maps with superior resolution and contrast compared to conventional OA tomography.

2. Results

2.1. Highly Absorbing Nanoscale Gold Yarn Balls

Porous gold nanoparticles with submicron size, herein referred to as gold yarn balls (AuYB), were synthesized with a one-step, high-yield synthesis procedure involving $HAuCl_4$ as a precursor, hydroquinone (HQ) for reduction, and polyvinylpyrrolidone (PVP) with different molecular weights as a surfactant, all in the presence of Ag^+ ions (**Figure 1a**, see methods for a detailed description). Successful nanoparticle formation with the desired shape was verified with scanning electron microscopy (SEM) images, revealing the highly convoluted surface (Figure 1b) and porous internal structure (Figure S1a–c, Supporting Information) of the particles. SEM images taken at different time points for which the synthesis procedure was preliminarily stopped showed the formation of Au-coated Ag nanocubes and subsequent gold overgrowth around these (Figure S1d, Supporting Information). Energy-dispersive X-ray spectroscopy (EDS) elemental analysis revealed the expected presence of gold and carbon from PVP, with an almost indistinct peak from silver and a peak from silicon related to the substrate on which particles were dropcasted (Figure 1c). SEM images further served to analyze the size distribution, demonstrating a dependence of AuYB size on the molar mass of the PVP molecules (40, 360, and 1300 kDa, Figure 1d). This could be explained by the fact that only monomer molarity was maintained during the synthesis procedure so that shorter PVP chains cover the particle surface. The larger steric hindrance of the long PVP chains can also be associated with the observed size variations.[43] UV–Vis-NIR spectroscopy demonstrated an increase in NIR absorption with particle size beyond the observed peak at ≈650 nm (Figure 1e; Figure S1e, Supporting Information). This is ascribed to the longer possible distances of the surface plasmon coupling both in-depth and along the superficial gold lamellae. Ligand exchange using SH-PEG-COOH solution was performed to further increase blood circulation times and improve biocompatibility. ζ-potentials measured before and after this step illustrated a slight increase of initially negative values related to PEG attachment for all particle sizes. Larger particles are preferred to enhance the per-particle OA signature, while NIR absorption is also of importance for increasing the achievable depth. Therefore, we focused on PEGylated AuYB synthesized in PVP40 (40 kDa) solution (AuYB40-PEG).

2.2. Biocompatibility and Biosafety

The biocompatibility and potential toxic effects of the AuYB40-PEG nanoparticles were assessed with a cell viability assay in
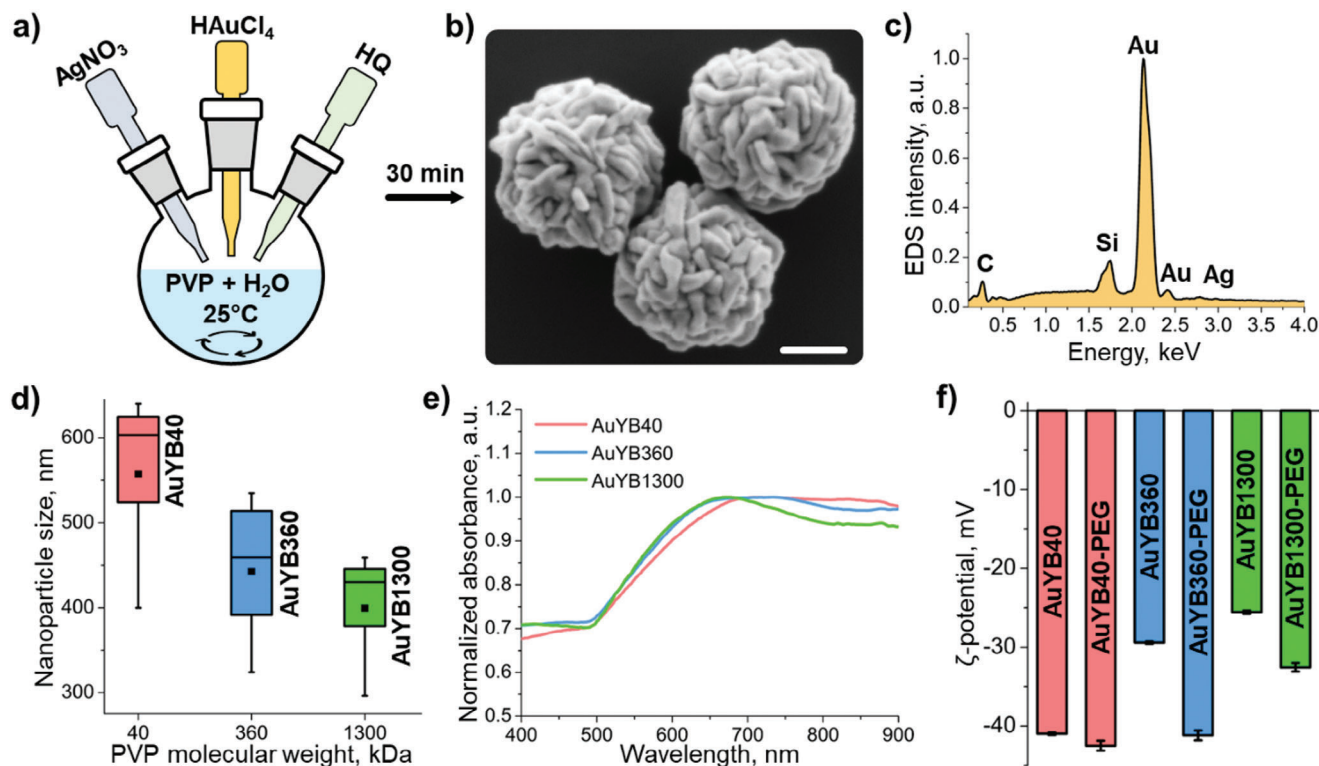
Figure 1. Synthesis and characterization of gold yarn balls (AuYB). a) Schematic representation of the AuYB synthesis procedure. b) SEM microphotograph of AuYB nanoparticles synthesized in PVP with 40 kDa molecular weight. Scalebar – 200 nm. c) EDS spectrum collected from the particles with peaks corresponding to different elements indicated. d) Size distribution of nanoparticles as a function of the molecular weight of PVP. e) UV–vis–NIR absorption spectra of the nanoparticles. f) ζ-potential values for nanoparticles before and after PEGylation.

Chinese hamster ovary (CHO), Murine macrophages (J774A.1) and primary human umbilical vein endothelial cells (HUVEC) cultured cells. This was done according to a standard alamarBlue assay after incubating the cells with AuYB40 nanoparticles at different concentrations (10^6 to 10^9 particles per mL) for 24 h (**Figure 2a**). The assay confirmed good cell viability, higher than 85%, for all concentrations (Figure 2b). Higher alamarBlue fluorescent signal values arguably indicate that cells are actively attempting to digest the internalized particles, thus resulting in increased metabolism. To assess the cell membrane damage, the cultures were incubated with AuYB40 nanoparticles for 24 h and then with alamarBlue for 4 h to highlight the cytoplasm and indicate that the cell is alive. After that, PBS (as negative control), DAPI or DAPI + 3% Triton X-100 solution in PBS were added and the cells were imaged using a confocal microscope to assess whether the nanoparticles induced any significant membrane damage to the cells (Figure 2c, see methods for the details). DAPI is known to be highly rejected by the undamaged cell membrane, thus no increase in the DAPI signal is expected while the cell is alive. Triton X-100 disrupts the membrane, causes cytoplasm leakage and provides a possibility for DAPI to stain the cell's nucleus. The acquired images demonstrated no significant difference between the control (PBS + alamarBlue + DAPI) and experimental (AuYB40 + alamarBlue + DAPI) groups for all the cell populations (Figure 2d; Figure S2a, Supporting Information). Note that some of the cells were stained with DAPI in the control samples, arguably because of a presence of a minor percentage of dead cells in the colony.

An hemolysis assay was carried out (Figure 2e; Figure S2b, Supporting Information) to assess RBC damage caused by AuYB40 nanoparticles at different concentrations with PBS as a negative control group and DDI as a positive control (see methods for more details). After 2 h of RBC incubation with various concentrations of nanoparticles, the hemolysis ratio turned out to be less than ≈10% in all cases. Note that the nanoparticle bolus is immediately diluted and distributed across the blood pool following intravenous injection in vivo, thus reducing the overall concentration of the contrast agent ≈20 times. The optical absorption spectrum of hemoglobin also remained unchanged, indicating no structural changes in the protein being in contact with AuYB (Figure S2b, Supporting Information). Minor laser damage of the RBCs was noted after irradiation of the AuYB/RBCs mixture with 2000 laser pulses at 800 nm and 20 mJ cm^{-2} per-pulse energy density (Figure S2c, Supporting Information). However, these results should be treated as an overestimation of the laser-induced hemolysis since no scattering layer was present between the light source and the sample, while attenuation of light in the skin, skull and brain tissues is expected in vivo.

The toxicity of AuYB was also tested in vivo in Swiss mice. The biochemical analysis of murine blood performed 11 days after intravenous administration of a suspension of AuYB40-PEG nanoparticles (100 µL bolus, 10^9 particles per mL) indicated no significant deviations from the control group administered with

ADVANCED
SCIENCE NEWS

www.advancedsciencenews.com
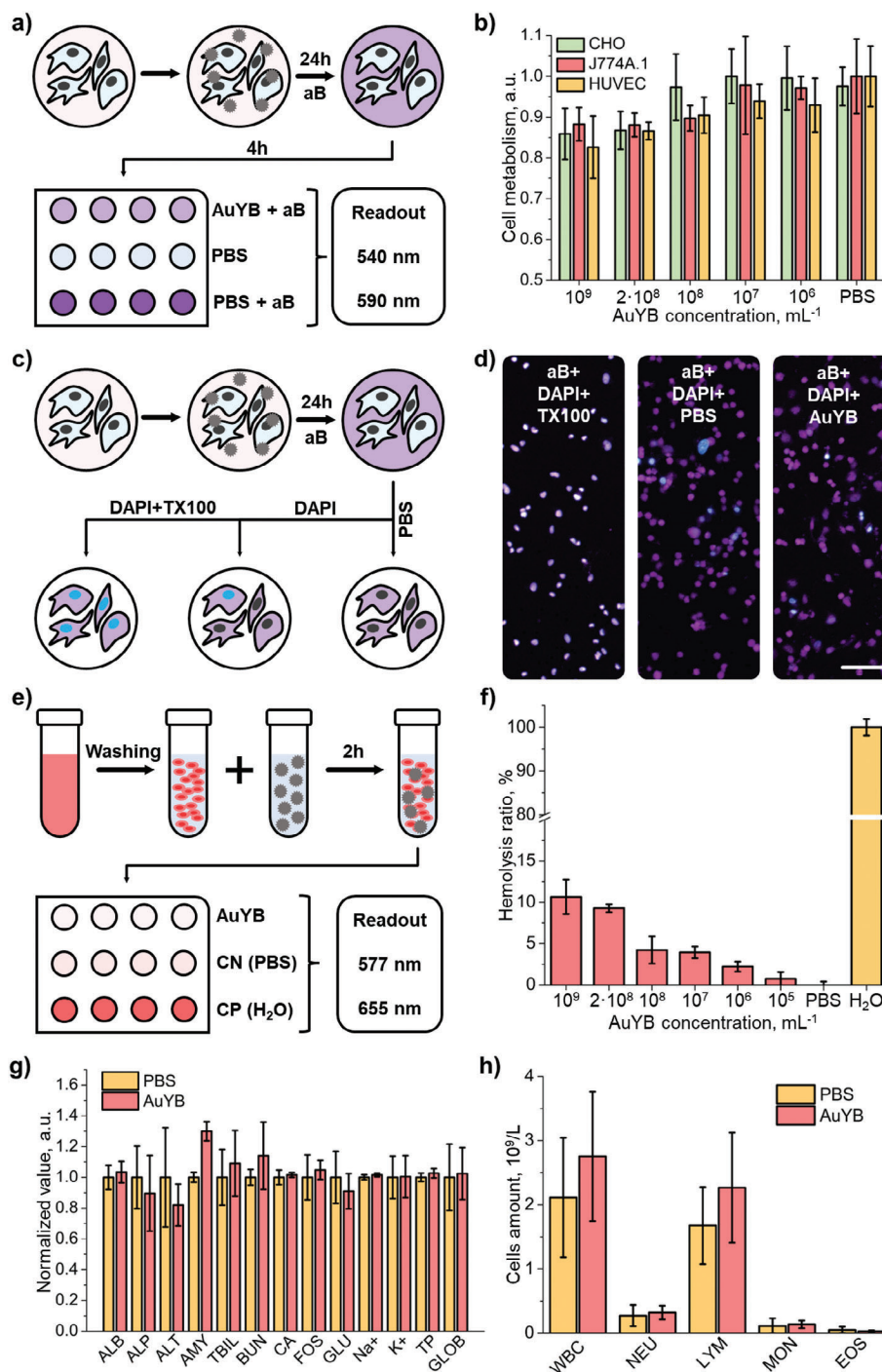
NANO · MICRO
small
www.small-journal.com

Figure 2. Biocompatibility and biosafety of PEGylated gold yarn balls (AuYB). A) Schematic representation of the alamarBlue cell metabolism assay steps: the cells are incubated with AuYB40-PEG for 24 h and then with alamarBlue (aB) for 4 h, followed by readouts at 540 nm excitation and 580 nm emission wavelength. b) Results of alamarBlue cell viability assay conducted on a Chinese hamster ovary (CHO), murine macrophages (J774A.1) and human umbilical vein endothelial cells (HUVEC) cell cultures fed with different concentrations of AuYB40-PEG. c) Schematic representation of the cell membrane damage test: the cells were first incubated with AuYB40-PEG, then with aB to highlight the cytoplasm and sequentially with PBS, DAPI, or Triton X-100 (TX100) + DAPI. d) Confocal microscopy images of the HUVEC cell culture incubated with aB + TX100 + DAPI, PBS + aB + DAPI, AuYB40-PEG + aB + DAPI. The blue color indicates the DAPI signal and violet color indicates the aB signal. Scalebar − 100 μm. g) Murine blood biochemistry taken on the 11th day post-injection of AuYB40-PEG nanoparticles or phosphate-buffered saline (PBS, control group): ALB – albumin, ALP – alkaline phosphatase, ALT – alanine transaminase, AMY – amylase, TBIL – total bilirubin, BUN – blood urea nitrogen, CA – calcium, PHOS – phosphates, GLU – glutamine, Na+ – sodium, K+ – potassium, TP – total protein, GLOB –globulin). h) Immune cell content of murine blood collected on the 11th days post-injection of AuYB40 nanoparticles or PBS (control group): WBC – white blood cells in total, Neu – neutrophils, Lym – lymphocytes, Mon – monocytes, Eos – eosinophils.

**ADVANCED
SCIENCE NEWS**

www.advancedsciencenews.com

**NANO · MICRO
small**

www.small-journal.com

phosphate-buffered saline (PBS). Specifically, similar levels of alkaline phosphatase, alanine transaminase, and blood urea nitrogen were observed, often used as indicators to assess kidney or liver damage (Figure 2g, Table S1, Supporting Information). Total bilirubin and total protein, associated with RBC destruction, also remained in the same range for both groups of mice. Similarly, the hematology analysis performed on day 11 following the administration of AuYB40-PEG or PBS revealed that the immune cell amount was also similar in both control groups, indicating no acute inflammation was produced in the organism (Figure 2h). No significant alterations in weight (Figure S3, Supporting Information), body condition, or behavior were observed for any of the mice.

2.3. Ultra-High-Speed Imaging of Plasmonic Cavitation

The fundamental mechanisms leading to ultrasound generation following exposure of plasmonic nanoparticles to a short-pulsed laser beam were investigated using an ultra-high-speed camera operating at 10 million frames per second. For this, a suspension of AuYB nanoparticles (10^6 particles per mL) was mixed with a 40/60 glycerol/water blood-mimicking medium and injected into a square glass capillary with 1×1 mm^2 cross-section. A custom-built 200x microscope was used to observe the particles (**Figure 3a**). The image focus was adjusted by maneuvering the capillary with a motorized 3D stage using a halogen lamp as a light source. A short-pulsed (≈6 ns) laser with wavelength 532 nm was aligned in a way that the beam profile was centered at the lateral side of the capillary with ≈17 mJ pulse^{-1} fluence, i.e., around the maximum permissible exposure in humans for visible light (20 mJ cm^{-2}).[44] Stray light from this beam was filtered out after the microscope objective so that it did not impact the camera readings. Acquisition of an image sequence consisting of 256 frames was synchronized with short-pulsed laser and flashlamp emissions using a delay generator (Figure 3b, see methods for details). Different phenomena were observed shortly after the excitation of the particles with the laser pulse. First, a plasmon-induced cavitation event (vapor bubble formation due to intense, localized heating caused by the excitation of surface plasmons) immediately took place (within 100 ns, 1 frame), reaching a diameter of ≈3.5 µm comparable to the size of well-established ultrasound contrast agents enabling per-particle detection (Figure 3c,d, Video S1, Supporting Information).[10] Bubble collapse due to outer pressure and gas cooling also happened in a very short time, with an interface speed during expansion and collapse in the order of 20 m^{-1}s. Indeed, the bubble was shown to contract to approximately the original size of the AuYB in less than 1 frame, resulting in particle fracturing and expelling of a piece of material from it (purple arrow in Figure 3c). Prior work tentatively suggests that material ejection could occur as a result of acoustic streaming inside the nanoparticles due to the rapid bubble collapse.[45–47] It was also observed that the bubble size increases with fluence (Figure S4a,b, Supporting Information). The bubble lifetime was shown to expand for several oscillations (Figure 3d, Video S1, Supporting Information). Accurate characterization of the rebound dynamics is however challenging because of the small size of the bubble after the first oscillation. The ability of AuYB to form vapor bubbles was also tested in the

cell interior. For this, a macrophage cell culture was co-incubated with AuYB40-PEG nanoparticles for 24 h to ensure internalization. Cells were subsequently detached from the 6-well plate with a scriber and injected into the 1×1 mm^2 glass capillary. PBS was used instead of the blood-mimicking fluid as outer medium and the laser fluence was set to ≈20 mJ cm^{-2}. Bubble formation took a significantly longer time for nanoparticles and nanoparticle clusters internalized into the cells than for particles within the blood-mimicking medium (400 ns vs 100 ns, Figure 3e). This could be explained by viscous forces inside the cells and the presence of a stiff cytoskeleton holding the bubble boundary and preventing fast expansion (Video S2, Supporting Information). The contraction process was also expanded (≈400 ns) relative to freely suspended particles in the blood-mimicking liquid, which could also be ascribed to the presence of the cytoskeleton.

2.4. Optical-Resolution Optoacoustic Microscopy

A custom-made optical-resolution optoacoustic microscopy (OR-OAM) setup capitalizing on coaxial light focusing and ultrasound detection with a single-element spherically-focused transducer was used for analyzing the OA signals generated by AuYB40-PEG nanoparticles. Specifically, a pulsed laser exciting the particles with a maximum of 20 mJ cm^{-2} laser fluence and 720 nm wavelength was used to study the temporal and frequency characteristics of the signals. First, the nanoparticle suspension (10^7 particles per mL) was mixed with 1% agar solution at 50 °C and drop-casted to an agar-coated polypropylene Petri dish to achieve a sparse distribution of OA sources. The Petri dish was then filled with DDI water and raster-scanned using the OR-OAM system (Figure 3f). The reconstructed OA image shows dispersed point-like sources across the field of view (FOV, Figure 3g). Heterogeneities in laser fluence associated to scattering in the agar gel and changes in beam diameter with depth resulted in a variability of the generated signal intensity ascribed to bubbles of different sizes being formed. A typical signal from one of the dots and its frequency content is shown in Figure 3h, corresponding to a main frequency of 4.7 MHz and full width at half maximum (FWHM) of 5 MHz. The dependence of the signal and its frequency spectrum on the excitation energy was also studied using the same OR-OAM setup (Figure S4c, Supporting Information). An increase in signal intensity and duration with increasing excitation energy was observed. This arguably indicates that the main source of the OA signals generated by the nanoparticles is the plasmonic bubble formation and collapse. The high resolution achieved with the OR-OAM system further allowed visualizing the distribution of particles within AuYB40-PEG-fed murine macrophage cells (Figure 3i). The outline of the cells could clearly be distinguished due to their high consumption of AuYB40-PEG nanoparticles.

2.5. Optoacoustic Tomography of Flowing Nanoparticles

Phantom experiments were carried out to investigate the limits of single-particle detection in the OA tomography setup. For this, a 280 µm inner diameter polyethylene tubing was coupled to a 512-element spherical array transducer via 1% agar gel (see methods
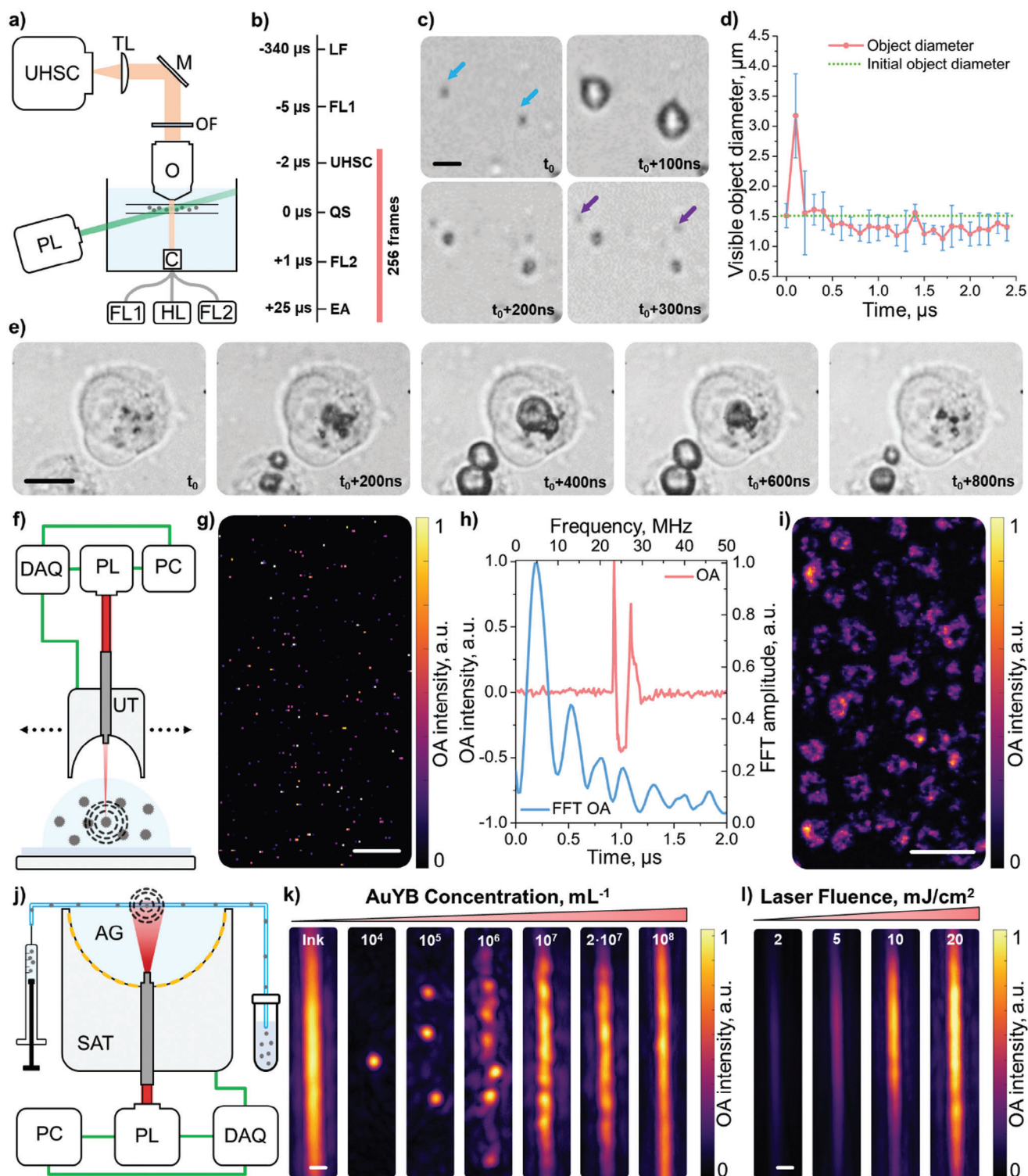
Figure 3. Ultra-high-speed imaging of bubble formation and collapse and corresponding optoacoustic (OA) signals. a) Ultra-high-speed camera imaging setup: UHSC – ultra-high-speed camera, TL – tube lens, M – mirror, OF – 532 nm long-pass optical filter, O – objective, PL – 532 nm pulsed laser, C – condenser, FL1 – flashlamp 1, HL – halogen lamp, FL2 – flashlamp 2. b) Acquisition sequence: LF – laser flashlamp, FL1 – flashlamp 1, UHSC – ultra-high-speed camera, QS – Q-switch, FL2 – flashlamp 2, EA – end of acquisition. c) Image sequence of AuYB40-PEG nanoparticles during plasmonic vaporization in a blood-mimicking solution after single laser pulse irradiation at ≈17 mJ cm^{-2} fluence: blue arrows – initial positions of the nanoparticles, violet arrows – ejected fraction of material. Scalebar – 2 μm. d) Time evolution of the visible diameter (microbubble and nanoparticle system) calculated for n = 4 nanoparticles. Error bars indicate the standard deviation of the measured size for different objects. e) Image sequence of nanoparticles-

**ADVANCED
SCIENCE NEWS**

www.advancedsciencenews.com

**NANO · MICRO
small**

www.small-journal.com

for details). Suspensions of AuYB40-PEG nanoparticles with different concentrations (10^4–10^8 particles per mL) were pumped through the tubing while excited using an 800 nm nanosecond-duration pulsed laser operating at 10 Hz repetition rate (Figure 3j, see methods for details). The tubing filled with India ink was also imaged as a reference of continuous contrast. Dots corresponding to sparsely distributed nanoparticles were observed when injecting relatively low concentrations (10^4–10^6 particles per mL). The OA image of the flowing beads started to turn into a "beading chain" at 10^7 particles per mL and into continuous-like contrast with undistinguishable particles at 10^8 particles per mL (Figure 3k). Note that the expected amount of nanoparticles in the effective FOV is N = 3, 30, 300, 3000, 30 000 and 60 000 for the injected concentrations, estimated considering a tubing 5-mm long and 280 µm in diameter ($\approx$0.3 µL volume). It should also be noted that the real amount of detected particles depends on the resolution of the OA system ($\approx$150 µm). On the other hand, the intensity of the OA signal from the particles was shown to depend on the deposited energy (Figure 3l), which is consistent with the experiments performed with the ultra-high-speed camera and the OR-OAM system, where the very faint signal at 2 mJ cm^{-2} excitation energy could be associated with the signal of the multiple nanoparticles either without the bubble formation or with a collapse of very fine bubble considering the lengths of the signal (Figure S4, Supporting Information).

2.6. Large-Scale High-Resolution Angiographic Optoacoustic Imaging

LOT relies on the detection of individual OA sources in the blood vessels, for which highly-absorbing particles with sizes in the order of a few micrometers have been required.[18,24] Considering that the size of the vapor bubbles being formed following laser excitation is similar to that of microbubbles producing sufficiently strong per-particle responses to be detectable with ultrasound scanners, AuYB40-PEG have potential as contrast agents for LOT. The feasibility of nanoparticle-based localization optoacoustic tomography (nanoLOT) was investigated by imaging the mouse brain vasculature following intravenous injection of a suspension of AuYB40-PEG nanoparticles (100 µL bolus, 10^8 particles per mL). For this, a custom-made OA tomographic imaging system based on a custom-made 512-element spherical array with $\approx$10 MHz detection bandwidth and an *ad-hoc* devised processing pipeline were used (**Figure 4a,b**, see methods for a detailed description). The mouse was anesthetized and placed in a prone position underneath a water tank enabling acoustic coupling between the mouse skin and the surface of the array. The reconstructed OA image at 800 nm excitation (isosbestic point of

hemoglobin) revealed major cerebral vessels[48] (Figure 4c). Notably, the OA resolution can be enhanced by capitalizing on the large bandwidth of the array to filter high ultrasound frequencies from the collected signals.[49,50] However, this compromises the achievable FOV, confining the resolution of microvascular structures to the central area of the spherical array. The inflow of AuYB40-PEG nanoparticles in the murine brain vasculature was observed shortly after tail vein administration. The nanoparticles stay in the blood pool without extravasation through the blood-brain barrier because of their size, thus facilitating angiographic visibility and resolution enhancement. Singular-value decomposition (SVD) filtering of subsets (100 frames) from the acquired OA sequence facilitated visualization of individual dots tentatively corresponding to individual nanoparticles in the blood vessels (see methods for a detailed description). Remarkably, the region where these dots were observed approximately matched the bandwidth-dependent FOV (Figure 4c), i.e., relatively low frequencies may facilitate reaching large-scale high-resolution images with LOT. The motion contrast optoacoustic (MC-OA) image, generated by combining normalized images from the SVD-filtered sequence corresponding to AuYB40-PEG-associated fluctuations, provided an enhanced visualization of cerebral vascular networks (Figure 4d). The LOT image was created by accumulating localized positions of particles ($\approx$60 000 points), thus enhancing the resolution of the MC-OA image and further resolving microvascular structures for a FOV unreachable with the high-frequency-based OA image (see Methods Section for further details). To further quantify the achieved image enhancement, AngioTool was used on the maximum intensity projection images along the depth axis and the amount of visible vessels was calculated. The results are presented in Figure 4f – the quantitative parameters like the vessel percentage area (VPA), total number of junctions (TNJ), total vessel length (TVL), and total number of endpoints (TNEP) were enhanced with MC-OA and LOT (Figure S5, Supporting Information). No significant damage was observed in the mice following acquisition of the sequence of images, with heart and breathing rates as well as other physiological parameters remaining unaltered.

3. Discussion and Conclusions

Nanoparticles are often preferred over microparticles as theranostic agents in biomedicine, particularly for intravenous administration, for several reasons. First, their smaller size allows for more efficient delivery of diagnostic or therapeutic substances to extravascular targets, thus minimizing side effects and increasing efficacy.[51–54] Additionally, nanoparticles can be engineered with precise surface modifications to enhance biocompatibility,

induced cavitation internalized by macrophages after a single laser pulse at $\approx$20 mJ cm^{-2} fluence. Scalebar – 10 µm. f) Optical-resolution optoacoustic microscopy (OR-OAM) imaging setup: DAQ – 2-channel data acquisition system, PL – 720 nm pulsed Laser, PC – personal computer, UT – single-element ultrasound transducer. g) OR-OAM image of the AuYB40-PEG nanoparticles embedded in 1% agar gel. Scalebar – 25 µm. h) Typical OA signal (red) and corresponding frequency content (blue) of the AuYB40-PEG excited at $\approx$20 mJ cm^{-2}. i) OR-OAM image of the murine macrophage cells that internalized AuYB40-PEG nanoparticles. Scalebar – 100 µm. j) OA tomography setup for phantom experiments: AG – 1% agar gel, SAT – 512-elements spherical array transducer, PC – personal computer, PL – 800 nm pulsed laser, DAQ – 512-channels data acquisition system. k) Dependence of the OA signal on the concentration of AuYB40-PEG particles flowing in the capillary tubing and exposed to $\approx$20 mJ cm^{-2}. The left image in the panel shows the polyethylene tubing filled with ink solution as a reference. In the other images, the concentration of AuYB40-PEG is increased logarithmically. Scalebar – 250 µm. l) Dependence of the OA signal of AuYB40-PEG for the maximum concentration on laser fluence. The fluence is calculated in mJ cm^{-2} and increased from left to right. The signal is normalized to the intensity for the maximum fluence.
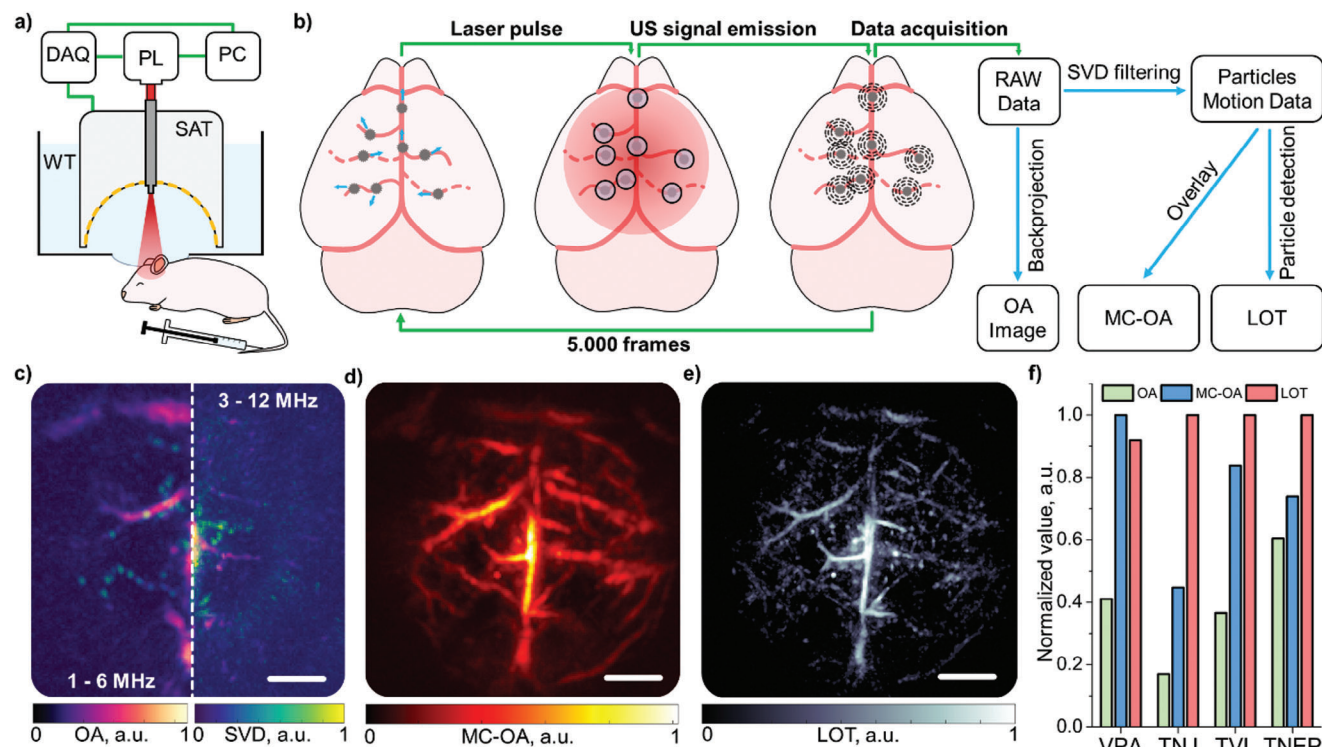
Figure 4. Super-resolution imaging of the murine brain. a) Lay-out of the mouse brain imaging setup: DAQ – data acquisition system, PL – near-infrared pulsed laser, PC – personal computer, WT – water tank, SAT – 512-elements spherical array transducer. b) Data processing pipeline: OA – optoacoustic image, SVD – singular value decomposition filter, MC-OA – motion contrast optoacoustic imaging, LOT – localization optoacoustic tomography. Dashed lines represent virtually invisible vessels using conventional OA tomography. c) OA image of the mouse brain vasculature reconstructed in the frequency ranges 1–6 MHz (left side) and 3–12 MHz (right side). Images of the particles reconstructed with the SVD-filtered data considering the same frequency ranges are superimposed. d) MC-OA image reconstructed from SVD-filtered data. e) LOT image reconstructed from particle tracks. Scalebars − 1 mm. f) Vessel quantification of OAT, MC-OA and LOT images performed with AngioTool: vessel percentage area (VPA), total number of junctions (TNJ), total vessel length (TVL), and total number of endpoints (TNEP) are indicated.

evade immune recognition, and increase circulation time in the bloodstream.[55,56] Reduced size also facilitates overcoming physiological barriers and ligand-receptor binding.[57] In vivo tracking of nanoparticles with existing deep-tissue biomedical imaging modalities relies on the cumulative signal from an increased particle concentration at specific locations. On the contrary, recent developments have demonstrated the feasibility of individual detection and tracking of particles with diameters in the order of a few micrometers. Particularly, individual microbubbles and light-absorbing microparticles have been shown to generate sufficiently strong ultrasound signals to be individually detected when excited with ultrasound pulses and short-pulsed lasers, respectively.[18,23,24,28,58,59] Herein, we have shown that laser excitation of AuYB40-PEG results in the formation of plasmonic cavitation bubbles with sizes in the order of individually-detectable microbubbles. This nano-to-micro conversion provides a means of generating sufficiently strong ultrasound signatures to be captured with piezoelectric arrays.[60,61] Gold nanoparticles are particularly efficient in converting light energy into heat upon exposure to specific wavelengths of light.[62,63] The proposed submicron-size AuYB feature surface plasmon resonances resulting in a relatively large optical cross-section and strongly enhanced near-infrared light absorption, thus facilitating contrast-enhanced OA imaging of optically-opaque biological tissues.

Bright-field microscopy images captured with an ultra-high-speed camera revealed the occurrence of transient nano-to-micro cavitation events triggered by laser excitation of AuYB40-PEG. Ultra-high-speed visualization of cavitation events provides valuable insights into the complex dynamics of bubble formation, growth, and collapse.[64–66] Cavitation dynamics in microbubbles and phase-change droplets subjected to rarefactional pressure have long been extensively studied, given the essential role they play in ultrasound medical imaging and therapy.[67] Bubble formation can also be induced using laser pulses with different pulse durations, which has also been visualized at a very high speed.[68,69] Bubble size relates to the amount of energy being converted, with bubble diameters up to hundreds of micrometers being reported. A dependence of bubble diameter on laser pulse energy was also observed in this work. Bubble diameters were confined to a few micrometers for per-pulse laser energy densities below safe limits for biological tissues. These are smaller than stable cavitation of clinically-approved microbubbles.[70] The small bubbles induced around AuYB40-PEG particles were also shown to expand and collapse in a very short time (<200 ns). Similar transient cavitation events could be tentatively produced around other types of nanoparticles and provide an explanation for the observed non-linear dependence of OA signal intensity on fluence.[71,72] Such events have also been exploited for

ADVANCED
SCIENCE NEWS

www.advancedsciencenews.com

NANO · MICRO

small

www.small-journal.com

super-resolution ultrasound mapping of the induced bubbles.[73] Moreover, the frequency content of the generated OA signals can be altered if cavitation events take place, which could be exploited for multiplexing nanoparticle-generated signals.[74] Even if individual detection of nanoparticles is not possible, particle-induced fluctuations in the images can enhance limited-view visibility and resolution as well as facilitate assessing blood flow.[75–78] Indeed, the MC-OA image was reconstructed from particle-induced fluctuations without the need for individual detection.

LOT offers an unparalleled three-fold advantage as a biomedical imaging tool. It breaks through the acoustic diffraction barrier to achieve three-dimensional microangiographic imaging, quantifies blood flow velocity, and effectively maps oxygen saturation.[18] By reducing the required particle size by an order of magnitude, nanoLOT can achieve this performance while effectively reducing the risk of embolisms that may arise from the aggregation of particles in the bloodstream. Small nanoparticles are often used to passively target tumors by capitalizing on the enhanced permeability and retention (EPR) effect.[79] The typical dimensions of endothelial fenestrations in the tumor vasculature are smaller than 200 nm, although apertures larger than 600 nm have been reported.[80] Tumor extravasation of AuYB40-PEG may then be produced, and can be further facilitated with the smaller diameter of AuYB360-PEG or AuYB1300-PEG. The feasibility of per-particle tracking of individual nanoparticles in vivo can shed new light on how these enter the tumor through endothelial cells and potentially exit the tumor microenvironment.[81] Bubble formation can also facilitate extravasation and further lead to therapeutic benefits, e.g., contributing to malignant cell damage or facilitating tumor ablation with high-intensity focused ultrasound (HIFU). Combined with the OA unique capability to quantify oxygen saturation, nanoLOT may additionally provide new insights into angiogenesis and hypoxia, two essential hallmarks of cancer.

In conclusion, plasmonic cavitation events in submicron-sized porous gold nanoparticles enable individual detection and tracking of nanoscale structures, potentially leading to transformative advancements in deep-tissue imaging. Being based on nanoparticle tracking, nanoLOT not only overcomes previous limitations of LOT related to the required size of particles, but also significantly reduces the risk of embolisms, a critical concern in longitudinal studies. This innovation paves the way for more detailed and safer super-resolution OA imaging of microvascular networks and potentially of extravascular tissues.

4. Experimental Section

Materials: Polyvinylpyrrolidone (PVP) of average molecular weight 40 kDa, 360 kDa, and 1300 kDa, silver nitrate ($AgNO_3$), chloroauric acid (HAuCl4), hydroquinone (HQ), Triton X-100, phosphate-buffered saline (PBS) and poly(ethylene glycol) 2-mercaptoethyl ether acetic acid (SH-PEG-COOH, Mn = 3500) were purchased from Sigma-Aldrich. Dulbecco's Modified Eagle's Medium (DMEM), alamarBlue cell assay kit, 4′,6-diamidino-2-phenylindole (DAPI), fetal bovine serum (FBS), 6-well plates and 96-well plates were purchased from Thermo Fisher Scientific Inc. Chinese hamster ovary (CHO) cells and J774A.1 murine macrophages were obtained from CLS Cell Lines Service GmbH. Primary human umbilical vein endothelial cells (HUVEC, pooled) and an endothelial cell growth medium kit were purchased from PromoCell GmbH. Double-deionized (DDI) water with an electrical resistivity of 18.2 MOhm·cm produced by a Millipore Milli-Q A10 system was used in all experiments. Isoflurane

was purchased from Abbott Laboratories, USA. Aquasonic ultrasound coupling gel was provided by Parker Laboratories Inc., USA.

Synthesis of Submicron Porous Gold Nanoparticles: Porous gold nanoparticles, also referred to as gold yarn balls (AuYB) in the manuscript, were synthesized according to a protocol modified from.[42] First, aqueous solutions of 30 mM HQ, 10 mM $AgNO_3$, 40 mM $HAuCl_4$, and 10 mg mL^{-1} PVP were prepared. Then, the reagents were mixed in the following sequence: 1) 4.5 mL of PVP solution was added to the 10 mL glass vials under vigorous stirring, 2) 320 µL of HQ was added and stirred for 30 s to ensure an equal distribution inside the flask, and 3) 60 µL of $AgNO_3$ solution was added followed by 200 µL of $HAuCl_4$ solution. The mixture was stirred for 3 minutes and left for 30 min for ripening. The particle suspension was then distributed into 2 mL Eppendorf tubes and washed 5 times with DDI water by 2 min centrifugation cycles at 2500 relative centrifugal force (rcf) to remove synthesis byproducts and unreacted components. The particles were then coated with SH-PEH-COOH using 1 mg mL^{-1} solution for 30 min, rinsed with DDI water and stored at 4 °C.

Scanning Electron Microscopy: Scanning Electron Microscopy (SEM) was used to assess the AuYB morphology and size distribution. For this, p-doped silicon chips were first washed in the ultrasonic bath with ethanol and DDI water. After that, 1 µL of each sample was drop-casted on the chip and dried at room temperature. Samples were imaged using a Schottky field emission SEM (Hitachi SU5000) in secondary electrons (SE) and backscattered electrons (BSE) contrast at 3 kV accelerating voltage. The elemental composition was analyzed using Energy Dispersive Spectroscopy (EDS), with signals generated at 10 kV accelerating voltage and collected by an Ultim Max silicon drift detector (Oxford Instruments pic, UK).

Size Distribution of the Nanoparticles: The size distribution of AuYB was analyzed using SE SEM microphotographs with image resolution 1280×960 (pixel size 27 nm) processed with a custom-designed software written in Python consisting of the following steps. First, a Gaussian blur filter was applied to denoise the image. This step effectively isolates particle boundaries without being hindered by subtle details. A user-configurable threshold value was then applied to the grayscale image to transform this into a binary image. Contours, representing the outlines of potential particles, were then detected within the binary image using the OpenCV (CV2) library. For each contour being identified, the rectangle with a minimum area that encapsulates this was estimated, which serves as a simplified representation of the particle's outline. The properties of the rectangles validated by the user, including major and minor axes, were extracted and stored in a matrix.

ζ-Potential Measurements: ζ-potential measurements were conducted using the Zetasizer Nano ZS90 (Malvern Panalytical, UK). All samples underwent a five-fold dilution with DDI water and were subsequently introduced into a folded capillary cell (DTS1070, Malvern). The acquired results were processed using Zetasizer software version 8.00. Measurements were done at a temperature of 25 °C and replicated three times to ensure reliability and accuracy.

Optical Spectroscopy: UV–vis spectroscopic analysis was performed by using a Tecan Infinite M200 well-plate reader in the wavelength range 350–850 nm in a Nunclon Delta Surface 96-well plate (Thermo Scientific, Denmark) with 200 µL of sample per well. The data was further analyzed using Origin 8.5.

Toxicity and Biosafety Studies: The biocompatibility of the nanoparticles was assessed using an alamarBlue assay performed on Chinese hamster ovary (CHO), murine macrophages (J774A.1), and primary human umbilical vein endothelial cells (HUVEC) cell cultures. Initially, cells were cultured in DMEM (CHO, J774A.1) supplemented with 10% FBS or endothelial cell growth medium (HUVEC) in a humidified incubator at 37 °C with 5% CO2. Subsequently, a 96-well plate was seeded with 10^4 cells per well, containing 200 µL of Phenol Red-free cell medium. Suspensions of AuYB40-PEG nanoparticles at different concentrations (from 10^6 to 10^9 particles per mL) were added to each row, with one row serving as the control. Following 24-hour incubation, cells were washed with PBS, and 20 µL of alamarBlue stock solution was added to each well following standard protocols. Cells were then left for 4 additional hours of incubation. Post-incubation, 100 µL of the cell-processed medium was transferred to a fresh 96-well plate to create a reading replica. This plate was loaded into

a well-plate reader (Infinite M200, Tecan), and the medium's fluorescence was measured at 540 nm excitation and 590 nm emission wavelengths.

The cell membrane damage caused by the nanoparticles was assessed using the following protocol. First, the cells (CHO, J774A.1 and HUVEC) were seeded in 6-well plates and cultured according to the protocol mentioned above in 2 mL of cell medium. For each cell culture, the cells in the upper row (3 wells) were then fed with 200 µL of $2 \cdot 10^8$ solution of AuYB40-PEG nanoparticles, and the lower row (3 wells) was supplemented with 200 µL of PBS as a control, following 24 h of incubation. After that, all the wells were rinsed 3 times with PBS and 200 µL of alamarBlue stock solution was added to each well. The cells were left in the incubator for 4 h to process the alamarBlue solution and turn it into the fluorescent form. The first column (2 wells) was supplemented with PBS and used as a negative control. The cells in the second column were rinsed with PBS again and 200 µL of 300 nM DAPI in PBS solution was added for 15 min. The cells were rinsed again to remove the excess of the dye. A 200 µL of 3% Triton X-100 in PBS (PBST) was added to the vital cells for 5 min and then rinsed 5 times with PBS to induce certain membrane damage. After that, 200 µL of 300 nM DAPI in PBS was added for 15 min and the cells were rinsed again. Every well was imaged using a confocal microscope (LSM 800, Zeiss) using 10x objective under 405 nm and 561 nm excitation for DAPI and alamarBlue fluorescence, respectively.

A hemolytic assay was used to test the potential damage of the RBCs by the AuYB40-PEG nanoparticles. First, 1 mL of murine blood was collected into the heparin-containing tube via cardiac puncture. After that, blood was diluted 10 times and rinsed with PBS 8 times via centrifugation at 1000 rcf for 7 min to isolate RBCs. Then, 0.5 mL of RBC solution was mixed with 0.5 mL of AuYB40-PEG at different concentrations (10^5 to 10^9 particles per mL) in PBS and incubated for 2 h at room temperature. Negative and positive controls were created by adding 0.5 mL of PBS and DDI water respectively. All the samples (RBCs + AuYB40-PEG, RBCs + PBS, RBCs + DDI water) were first centrifuged at 1000 rcf for 7 min to remove the RBCs and then at 10.000 rcf for 5 min to remove the AuYB40-PEG nanoparticles affecting the absorbance readings. The samples were placed in the 96-well plate and their absorbance was measured at 577 nm and 655 nm as reference. Absorbance in the range of 350–850 nm was also collected to ensure that hemoglobin remained unchanged. The overall hemolytic ratio was calculated according to the following equation:

$$HR = 100\% \times \left(OD_{test} - OD_{negative\ control} \right)$$
$$/ \left(OD_{positive\ control} - OD_{negative\ control} \right) \quad (1)$$

In addition, an assessment of the induced laser damage on the RBCs+AuYB40-PEG mixture was studied. A 0.5 mL suspension of AuYB40-PEG (10^8 particles per mL) in PBS was mixed with 0.5 mL of RBCs and exposed to 2000 laser pulses at 10 Hz repetition rate, 800 nm wavelength, with ≈20 mJ cm^{-2} per-pulse energy density. The same procedure was performed for negative and positive controls, and the hemolytic ratio was calculated according to the protocol mentioned above.

The biosafety of the nanoparticles was further evaluated in Swiss mice (n = 8, 4 males and 4 females, 7 weeks old). These mice were randomly divided into control (n = 4) and experimental (n = 4) groups, 2 males and 2 females per group, and intravenously injected with a single dose (100 µL) of PBS or the nanoparticle suspension (10^9 particles per mL), respectively. Mice were scored and weighted for 11 days post-intravenous administration and eventually euthanized. Hematological analysis of blood samples was done on day 11 post-injection using a BC5000-Vet analyzer (Mindray). Clinical biochemistry was performed on collected serum samples at the final time point (day 11 post-injection) using a VetScan VS2 analyzer (Zoetis). This biosafety study adhered to Spanish and European regulations and received approval from the Xunta de Galicia.

Ultra-High-Speed Imaging of Plasmonic Cavitation: The underlying mechanism of ultrasound generation by the AuYB upon short-pulsed laser exposure was investigated with an ultra-high-speed camera. For this, a modified version of the previously reported bright-field microscopy system was used.[82] An aqueous suspension of AuYB was injected into a glass

capillary with 1 mm^2 square cross-section, and placed in a holder connected to 3-axis translation stages within a water tank. The optical setup included a microscopy objective (CFI Plan 100XC W, Nikon), a 532 nm OD4 filter (#67 128, Edmund optics), a tube lens (TL400-A, Thorlabs), a redirecting mirror, and a Shimadzu Hyper Vision HPV-X2 camera. Bright-field images were acquired via trans-illumination of the capillary with 2 xenon flashlamps (MVS-7010, EG&G, 15 µs duration), while a 532 nm Q-switch laser (New Wave Research Solo PIV 120, 6 ns pulse, 5 mm beam diameter) was directed from the lateral side of the capillary to excite the nanoparticles. Acquisition of a sequence of images was synchronized with the laser flashlamp trigger using a delay generator (Stanford Research Systems DG645) which, in turn, triggered the Q-switch at a specific delay. Synchronization of laser emission and acquisition of images was performed as follows. The flashlamp pumping of the short-pulsed laser was used as a master trigger for the delay generator. Prior of 5 µs to the emission of the laser pulse, the first xenon flashlamp used as a light source for image acquisition was triggered. The camera was triggered 3 µs later so that image acquisition started when the first flashlamp reached maximum intensity. The second xenon flashlamp, required as additional light source for a relatively large image acquisition time, was triggered 1 µs after short-pulsed laser emission. In this manner, illumination was maintained for 20 µs from the beginning of the camera recording. Acquisition was finished approximately 30 µs after the emission of the laser pulse and the entire sequence of 256 frames (100 ns step) was transferred to a PC. Variations in laser Q-switch delays enabled adjusting the per-pulse energy, providing flexibility to study particle behavior at different energy levels or align energy levels with values relevant to in vivo studies. Specifically, AuYB nanoparticles were excited at pulse energies of 10, 17, 30, and 62 mJ, corresponding to laser fluences of 12.8, 21.7, 32, and 64 mJ cm^{-2}, respectively. Data analysis was performed using ImageJ 1.54 h.

OR-OAM Characterization of the Nanoparticles: The OA response produced by AuYB40-PEG nanoparticles was characterized by mixing 1 mL particle suspension ($2 \cdot 10^7$ particles per mL) with 1 mL of 2% heated agar solution. The bottom of the polypropylene Petri dish was first coated with a 2 mm layer of 1% agar and then 4 µL droplets of AuYB40-PEG-in-1% agar solution were drop-casted. After 10 min of agar solidification at 4 °C, the Petri dish was filled with DDI water and samples were imaged with a previously reported OR-OAM system.[83] A nanosecond dye laser (pulse duration ≈7 ns) tuned to an optical wavelength of 720 nm and operated at a maximum pulse repetition rate of 6 kHz (Sirah Lasertechnik GmbH) was used for OA excitation. The per-pulse laser energy was adjusted within the range of 300–1000 nJ pulse^{-1}, corresponding to fluence levels of 10–30 mJ cm^{-2} at the focal light spot. The laser beam was guided through a single-mode fiber with a gradient-index lens on the tip, which was inserted through the central aperture of a coaxially aligned focused poly(vinylidene difluoride) (PVDF) ultrasound transducer with 25 MHz central frequency and ≈30 MHz bandwidth. The transducer was raster-scanned across a 1 mm × 1 mm sample area with 1 µm steps size in both x and y directions. The OA signal and photodiode signal for fluence normalization were digitized via a double-channel data acquisition system (Spectrum Instrumentation GmbH), and processed using Matlab 2022b (Mathworks). The frequency components of the spectrum were calculated using a Fast Fourier Transform of the entire signal (2 µs length).

Optoacoustic Imaging of the Flowing Nanoparticles: The dependence of the OA signal on the concentration of AuYB40-PEG nanoparticles was studied using a simplistic flow phantom. A polyethylene tubing with 280 µm inner diameter was placed over a custom-made 512-element spherical transducer array (10 MHz central frequency, 30 mm focal distance) featuring a central aperture to guide the laser light. The cavity of the transducer was filled with 1% agar gel to ensure acoustic coupling of the tubing. Nanoparticle suspensions with different concentrations (10^4–10^8 particles per mL) were pumped through the capillary using a syringe pump (NE-300, New Era Pump Systems Inc., 100 µl min^{-1}, corresponding to ≈25 mm^{-1}s flow velocity) and excited using a 10 Hz repetition rate optical parametric oscillator (OPO)-based laser tuned to 800 nm wavelength and providing ≈20 mJ cm^{-2} per-pulse energy density at the tubing. The optoacoustic data of (1008 samples x 512 elements) x 1000 time points

was reconstructed using a self-developed GPU-based back projection algorithm using Matlab 2022b (Mathworks).[84]

Animal Imaging Experiments: Female athymic nude mice ($\approx$25 g body weight, 8 weeks old) were used for OA imaging and tracking of AuYB in vivo. For this, the animals were anaesthetized with isoflurane (5% v/v for induction and 1.5% v/v for maintenance, Abbott, Cham, Switzerland) in an oxygen/air mixture (100/400 mL mi^{-1}n). The mice were housed in ventilated cages inside a temperature-controlled (21 ± 1 °C) and humidity-controlled (55 ± 10%) room under an inverted 12 h dark/light cycle. Pelleted food and water were provided ad libitum. All experiments were performed following the Swiss Federal Act on Animal Protection and were approved by the Cantonal Veterinary Office Zürich.

For OA imaging of the brain, the eyes were covered with turbid vet ointment and the head was fixed in a stereotactic frame with plastic ear bars. The mouse was placed in a prone position on a heating pad covered with soft tissue to maintain a constant body temperature (37 °C). A catheter was inserted in the tail vein and a 100 µL bolus of an AuYB suspension (10^8 particles per mL) was injected into the bloodstream.

Optoacoustic Imaging of the Mouse Brain: OA images of the mouse brain were acquired with a custom-made 512-element spherical array with 10 MHz central frequency and 30 mm focal distance (Imasonic SaS, Voray, France).[85] OA excitation was provided with an optical parametric oscillator (OPO)-based laser tuned to 800 nm wavelength and 10 Hz pulse repetition frequency. Parallel acquisition of all 512 OA signals for all array elements was performed for 10 min (6000 frames): Thirty second before injection of AuYB, 30 s during injection, and 5 min after injection. The laser beam was guided to the mouse head through the central aperture of the transducer using a custom-made fibre bundle (Lightguide, Germany) composed of solitary silica fibres with NA of 0.5. The energy density at the mouse skin was approximately 20 mJ cm^{-2}. OA images were reconstructed for the frames before injection considering the bandpass Butterworth filter with cut-off frequencies 1–6 MHz and 3–12 MHz within 8×8×4 mm^3 (W x L x D) at 25 µm pixel size.

Motion Contrast and Localization Optoacoustic Tomography: MC-OA and LOT images were reconstructed from the acquired datasets following a procedure adapted from.[18,23] In brief, the raw signals were first filtered with a bandpass Butterworth filter with cut-off frequencies of 1–6 MHz corresponding to the main band of the nanoparticle emission. Then, noise, comprised of slow tissue and breathing motion and fast noise related to the spatial components was removed by single-value decomposition (SVD) filtering. For this, the Casorati matrix of 100-frame subsets with dimensions (1008×512) x 100 was filtered by setting an eigenvectors range of 31–80, corresponding to the signals from fast-moving AuYB. The SVD-filtered signals were then reconstructed as 3D-frames containing the particle-related spheroids with 320×320×320 voxels, and summed up along the temporal axis for the entire acquisition to get the motion contrast optoacoustic (MC-OA) image.

Isolated nanoparticles appear in the image as the local point spread function (PSF) due to their high absorption and sub-resolution size. In each SVD-filtered and reconstructed frame, local intensity maxima were first detected using a weighted centroid approximation with the top border of 25 localized points per frame, and small regions centered at these maxima were correlated (with correlation coefficients above 0.3) to an empirical PSF of the imaging system. Localization of these correlated particles was then further refined using a local quadratic fitting of the intensity maxima, and their positions were stored. The resulting LOT image was created by overlaying the particle positions and a corresponding PSF for each time frame of the acquisition.

The performance of OA, MC-OA and LOT was assessed using AngioTool, with quantitative parameters such as vessel percentage area (VPA), total number of junctions (TNJ), total vessel length (TVL), and total number of endpoints (TNEP) being calculated.

Supporting Information

Supporting Information is available from the Wiley Online Library or from the author.

Conflict of Interest

The authors declare no conflict of interest.

Data Availability Statement

The data that support the findings of this study are available from the corresponding author upon reasonable request.

[1] L. Schermelleh, A. Ferrand, T. Huser, C. Eggeling, M. Sauer, O. Biehlmaier, G. P. C. Drummen, *Nat. Cell Biol.* **2019**, *21*, 72.

[2] P. Fu, W. Cao, T. Chen, X. Huang, T. Le, S. Zhu, D.-W. Wang, H. J. Lee, D. Zhang, *Nat. Photonics* **2023**, *17*, 330.

[3] G. R. Heath, E. Kots, J. L. Robertson, S. Lansky, G. Khelashvili, H. Weinstein, S. Scheuring, *Nature* **2021**, *594*, 385.

[4] Q. Zhou, D. Nozdriukhin, Z. Chen, L. Glandorf, U. A. T. Hofmann, M. Reiss, L. Tang, X. L. Deán-Ben, D. Razansky, *Adv. Sci.* **2023**, *10*, 2204782.

[5] J. Shi, Y. Tang, J. Yao, *Quantitat. Imag. Med. Surg.* **2018**, *8*, 724.

[6] K. Christensen-Jeffries, O. Couture, P. A. Dayton, Y. C. Eldar, K. Hynynen, F. Kiessling, M. O'Reilly, G. F. Pinton, G. Schmitz, M.-X. Tang, M. Tanter, R. J. G. van Sloun, *Ultrasound Med. Biol.* **2020**, *46*, 865.

[7] K. Prakash, B. Diederich, R. Heintzmann, L. Schermelleh, *Philos. Trans. R. Soc. A* **2022**, *380*, 20210110.

[8] E. Betzig, G. H. Patterson, R. Sougrat, O. W. Lindwasser, S. Olenych, J. S. Bonifacino, M. W. Davidson, J. Lippincott-Schwartz, H. F. Hess, *Science* **2006**, *313*, 1642.

[9] M. J. Rust, M. Bates, X. Zhuang, *Nat. Methods* **2006**, *3*, 793.

[10] C. Errico, J. Pierre, S. Pezet, Y. Desailly, Z. Lenkei, O. Couture, M. Tanter, *Nature* **2015**, *527*, 499.

[11] T. Opacic, S. Dencks, B. Theek, M. Piepenbrock, D. Ackermann, A. Rix, T. Lammers, E. Stickeler, S. Delorme, G. Schmitz, F. Kiessling, *Nat. Commun.* **2018**, *9*, 1527.

[12] C. Demené, J. Robin, A. Dizeux, B. Heiles, M. Pernot, M. Tanter, F. Perren, *Nat. Biomed. Eng.* **2021**, *5*, 219.

[13] H. Assi, R. Cao, M. Castelino, B. Cox, F. J. Gilbert, J. Gröhl, K. Gurusamy, L. Hacker, A. M. Ivory, J. Joseph, F. Knieling, M. J. Leahy, L.

ADVANCED
SCIENCE NEWS

www.advancedsciencenews.com

NANO · MICRO
small
www.small-journal.com

Lilaj, S. Manohar, I. Meglinski, C. Moran, A. Murray, A. A. Oraevsky, M. D. Pagel, M. Pramanik, J. Raymond, M. K. A. Singh, W. C. Vogt, L. Wang, S. Yang, Members of IPASC, S. E. Bohndiek, *Photoacoustics* **2023**, *32*, 100539.

[14] X. Deán-Ben, S. Gottschalk, B. Mc Larney, S. Shoham, D. Razansky, *Chem. Soc. Rev.* **2017**, *46*, 2158.

[15] B. Hindelang, T. Nau, L. Englert, A. Berezhnoi, F. Lauffer, U. Darsow, T. Biedermann, K. Eyerich, J. Aguirre, V. Ntziachristos, *Sci. Transl. Med.* **2022**, *14*, eabm8059.

[16] J. Yao, C. Kim, M. Kolios, S. Hu, *Photoacoustics* **2023**, *32*, 100541.

[17] D. Jiang, L. Zhu, S. Tong, Y. Shen, F. Gao, F. Gao, *J. Biomed. Opt.* **2024**, *29*, S11513.

[18] X. L. Deán-Ben, J. Robin, D. Nozdriukhin, R. Ni, J. Zhao, C. Glück, J. Droux, J. Sendón-Lago, Z. Chen, Q. Zhou, B. Weber, S. Wegener, A. Vidal, M. Arand, M. El Amki, D. Razansky, *Nat. Commun.* **2023**, *14*, 3584.

[19] D. Razansky, J. Klohs, R. Ni, *Eur. J. Nuclear Med. Mol. Imag.* **2021**, *48*, 4152.

[20] L. Lin, L. V. Wang, *Nat. Rev. Clin. Oncol.* **2022**, *19*, 365.

[21] A. Karlas, M. A. Pleitez, J. Aguirre, V. Ntziachristos, *Nat. Rev. Endocrinol.* **2021**, *17*, 323.

[22] X. L. Dean-Ben, D. Razansky, *Light: Sci. Appl.* **2018**, *7*, 18004.

[23] D. Nozdriukhin, S. K. Kalva, W. Li, A. Yashchenok, D. Gorin, D. Razansky, X. L. Deán-Ben, *ACS Appl. Mater. Interfaces* **2021**, *13*, 48423.

[24] D. Nozdriukhin, S. Lyu, J. Bonvin, M. Reiss, D. Razansky, X. L. Dean-Ben, Copper phosphate micro-flowers coated with indocyanine green and iron oxide nanoparticles for in vivo localization optoacoustic tomography and magnetic actuation. arXiv preprint arXiv:2402.06749 **2024**.

[25] O. Degtyaruk, D. Nozdriukhin, D. Razansky, X. L. Deán-Ben, *Opt. Lett.* **2021**, *46*, 4350.

[26] Y. Hu, Y. Sun, C. Wan, X. Dai, S. Wu, P.-C. Lo, J. Huang, J. F. Lovell, H. Jin, K. Yang, *J. Nanobiotechnol.* **2022**, *20*, 189.

[27] S. Nejati, E. M. Vadeghani, S. Khorshidi, A. Karkhaneh, *Eur. Polym. J.* **2020**, *122*, 109353.

[28] A. Dasgupta, T. Sun, R. Palomba, E. Rama, Y. Zhang, C. Power, D. Moeckel, M. Liu, A. Sarode, M. Weiler, A. Motta, C. Porte, Z. Magnuska, A. Said Elshafei, R. Barmin, A. Graham, A. McClelland, D. Rommel, E. Stickeler, F. Kiessling, R. M. Pallares, L. De Laporte, P. Decuzzi, N. McDannold, S. Mitragotri, T. Lammers, *Proc. Natl. Acad. Sci. USA* **2023**, *120*, 2218847120.

[29] Y.-S. Chen, Y. Zhao, S. J. Yoon, S. S. Gambhir, S. Emelianov, *Nat. Nanotechnol.* **2019**, *14*, 465.

[30] R. García-Álvarez, L. Chen, A. Nedilko, A. Sánchez-Iglesias, A. Rix, W. Lederle, V. Pathak, T. Lammers, G. von Plessen, K. Kostarelos, L. M. Liz-Marzán, A. J. C. Kuehne, D. N. Chigrin, *ACS Photonics* **2020**, *7*, 646.

[31] J.-S. Wi, J. Kim, M. Y. Kim, S. Choi, H. J. Jung, C. Kim, H.-K. Na, *RSC Adv.* **2023**, *13*, 9441.

[32] M. Grzelczak, J. Pérez-Juste, P. Mulvaney, L. M. Liz-Marzán, *Chem. Soc. Rev.* **2008**, *37*, 1783.

[33] A. K. Pearce, T. R. Wilks, M. C. Arno, R. K. O'Reilly, *Nat. Rev. Chem.* **2021**, *5*, 21.

[34] R. Zhang, S. Thöroe-Boveleth, D. N. Chigrin, F. Kiessling, T. Lammers, R. M. Pallares, *J. Nanobiotechnol.* **2024**, *22*, 115.

[35] D. M. Solís, J. M. Taboada, F. Obelleiro, L. M. Liz-Marzán, F. J. García de Abajo, *ACS Nano* **2014**, *8*, 7559.

[36] D. Kumar, J. Y. Lee, M. J. Moon, W. Kim, Y. Y. Jeong, C. H. Park, C. S. Kim, *Biomater. Sci.* **2022**, *10*, 2394.

[37] M. Guo, J. He, Y. Li, S. Ma, X. Sun, *J. Hazard. Mater.* **2016**, *310*, 89.

[38] A. Kosinova, D. Wang, E. Baradács, B. Parditka, T. Kups, L. Klinger, Z. Erdélyi, P. Schaaf, E. Rabkin, *Acta Mater.* **2017**, *127*, 108.

[39] G. Liu, K. Li, Y. Zhang, J. Du, S. Ghafoor, Y. Lu, *Appl. Surf. Sci.* **2020**, *527*, 146807.

[40] S. Dong, L. Yi, L. Cheng, S. Li, W. Yang, Z. Wang, S. Jiang, *Sci. Rep.* **2020**, *10*, 16555.

[41] W. Li, L. Kuai, L. Chen, B. Geng, *Sci. Rep.* **2013**, *3*, 2377.

[42] S. Pediredd, H. K. Lee, W. W. Tjiu, I. Y. Phang, H. R. Tan, S. Q. Chua, C. Troadec, X. Y. Ling, *Nat. Commun.* **2014**, *5*, 4947.

[43] C. Pratthana, K.-F. Aguey-Zinsou, *Appl. Sci.* **2022**, *12*, 4742.

[44] R. N. Pritzker, T. E. Rohrer, in *Handbook of Lasers in Dermatology*, Springer, London, p. 11, **2014**.

[45] M. Dular, T. Požar, J. Zevnik, *Wear* **2019**, *418*, 13.

[46] G. Lajoinie, E. Gelderblom, C. Chlon, M. Böhmer, W. Steenbergen, N. de Jong, S. Manohar, M. Versluis, *Nat. Commun.* **2014**, *5*, 3671.

[47] T. Takata, M. Enoki, P. Chivavibul, A. Matsui, Y. Kobayashi, *Mater. Trans.* **2016**, *57*, 1776.

[48] I. Gezginer, Z. Chen, H. A. Yoshihara, X. L. Deán-Ben, D. Razansky, *Photoacoustics* **2023**, *31*, 100522.

[49] P. Subochev, X. L. Deán-Ben, Z. Chen, A. Orlova, D. Razansky, presented at Photons Plus Ultrasound: Imaging and Sensing, SPIE, Bellingham **2021** 129–134.

[50] A. Longo, D. Jüstel, V. Ntziachristos, *IEEE Trans. Med. Imag.* **2022**, *41*, 3373.

[51] P. Cheng, K. Pu, *Nat. Rev. Mater.* **2021**, *6*, 1095

[52] R. Weissleder, M. Nahrendorf, M. J. Pittet, *Nat. Mater.* **2014**, *13*, 125.

[53] T. I. Janjua, Y. Cao, C. Yu, A. Popat, *Nat. Rev. Mater.* **2021**, *6*, 1072.

[54] H. Tao, T. Wu, M. Aldeghi, T. C. Wu, A. Aspuru-Guzik, E. Kumacheva, *Nat. Rev. Mater.* **2021**, *6*, 701.

[55] Z. Li, X. Shan, Z. Chen, N. Gao, W. Zeng, X. Zeng, L. Mei, *Adv. Sci.* **2021**, *8*, 2002589.

[56] G. Sanità, B. Carrese, A. Lamberti, *Front. Mol. Biosci.* **2020**, *7*, 587012.

[57] Z. R. Goddard, M. J. Marín, D. A. Russell, M. Searcey, *Chem. Soc. Rev.* **2020**, *49*, 8774.

[58] Y. Shin, M. R. Lowerison, Y. Wang, X. Chen, Q. You, Z. Dong, M. A. Anastasio, P. Song, *Nat. Commun.* **2024**, *15*, 2932.

[59] N. Renaudin, S. Pezet, N. Ialy-Radio, C. Demene, M. Tanter, *Sci. Rep.* **2023**, *13*, 11477.

[60] E. Huynh, B. Y. C. Leung, B. L. Helfield, M. Shakiba, J.-A. Gandier, C. S. Jin, E. R. Master, B. C. Wilson, D. E. Goertz, G. Zheng, *Nat. Nanotechnol.* **2015**, *10*, 325.

[61] K. Wilson, K. Homan, S. Emelianov, *Nat. Commun.* **2012**, *3*, 618.

[62] L. Liz-Marzán, in *Colloidal Synthesis of Plasmonic Nanometals*, CRC Press, Boca Raton **2020**.

[63] C. Gellini, A. Feis, *Photoacoustics* **2021**, *23*, 100281.

[64] P. S. Sheeran, T. O. Matsunaga, P. A. Dayton, *Phys. Med. Biol.* **2013**, *58*, 4513.

[65] O. Supponen, D. Obreschkow, M. Tinguely, P. Kobel, N. Dorsaz, M. Farhat, *J. Fluid Mechan.* **2016**, *802*, 263.

[66] H. Li, X. Li, G. Collado-Lara, K. R. Lattwein, F. Mastik, R. Beurskens, A. F. W. van der Steen, M. D. Verweij, N. de Jong, K. Kooiman, *Ultrasound Med. Biol.* **2023**, *49*, 388.

[67] Z. Izadifar, P. Babyn, D. Chapman, *J. Med. Biol. Eng.* **2019**, *39*, 259.

[68] D. Han, R. Yuan, R. Jiang, X. Geng, Q. Zhong, Y. Zhang, Z. Yao, F. Wang, *Ultrason. Sonochem.* **2021**, *78*, 105733.

[69] M. Vassholz, H. P. Hoeppe, J. Hagemann, J. M. Rosselló, M. Osterhoff, R. Mettin, T. Kurz, A. Schropp, F. Seiboth, C. G. Schroer, M. Scholz, J. Möller, J. Hallmann, U. Boesenberg, C. Kim, A. Zozulya, W. Lu, R. Shayduk, R. Schaffer, A. Madsen, T. Salditt, *Nat. Commun.* **2021**, *12*, 3468.

[70] E. Stride, *Cerebrovas. Dis.* **2009**, *27*, 1.

[71] C.-W. Wei, M. Lombardo, K. Larson-Smith, I. Pelivanov, C. Perez, J. Xia, T. Matula, D. Pozzo, M. O'Donnell, *Appl. Phys. Lett.* **2014**, *104*, 033701.

[72] M. I. P. Mendes, C. D. F. Coelho, F. A. Schaberle, M. J. Moreno, M. J. F. Calvete, L. G. Arnaut, *RSC Adv.* **2023**, *13*, 35040.

2404904 (12 of 13)

[73] G. P. Luke, A. S. Hannah, S. Y. Emelianov, *Nano Lett.* **2016**, *16*, 2556.

[74] S. Kellnberger, D. Soliman, G. J. Tserevelakis, M. Seeger, H. Yang, A. Karlas, L. Prade, M. Omar, V. Ntziachristos, *Light:Sci. Appl.* **2018**, *7*, 109.

[75] X. L. Deán-Ben, L. Ding, D. Razansky, *Opt. Lett.* **2017**, *42*, 827.

[76] T. Chaigne, B. Arnal, S. Vilov, E. Bossy, O. Katz, *Optica* **2017**, *4*, 1397.

[77] Y. Zhang, J. Olick-Gibson, A. Khadria, L. V. Wang, *Nat. Biomed. Eng.* **2024**, *8*, 701.

[78] Y. Tang, S. Tang, C. Huang, P. Klippel, C. Ma, N. Caso, S. Chen, Y. Jing, J. Yao, *Photoacoustics* **2023**, *29*, 100450.

[79] A. Nel, E. Ruoslahti, H. Meng, *ACS Publicat.* **2017**, *11*, 9567.

[80] N. Alasvand, A. M. Urbanska, M. Rahmati, M. Saeidifar, P. S. Gungor-Ozkerim, F. Sefat, J. Rajadas, M. Mozafari, *Multifunctional systems for combined delivery, biosensing and diagnostics*, Elsevier, **2017**, pp. 245–259.

[81] L. N. M. Nguyen, Z. P. Lin, S. Sindhwani, P. MacMillan, S. M. Mladjenovic, B. Stordy, W. Ngo, W. C. W. Chan, *Nat. Mater.* **2023**, *22*, 1261.

[82] M. Cattaneo, O. Supponen, *Soft Matter* **2023**, *19*, 5925.

[83] J. Rebling, M. Ben-Yehuda Greenwald, M. Wietecha, S. Werner, *Adv. Sci.* **2021**, *13*, 2004226.

[84] A. Ozbek, X. L. Deán-Ben, D. Razansky, *IEEE Transactions on Medical Imaging*, **2013**, *32*, 2050.

[85] X. L. Deán-Ben, G. Sela, A. Lauri, M. Kneipp, V. Ntziachristos, G. G. Westmeyer, S. Shoham, D. Razansky, *Light: Sci. Appl.* **2016**, *5*, 16201.